ACS Sustainable Chemistry & Engineering

pubs.acs.org/journal/ascecg

Research Article

Hexafluorosilicic Acid (FSA): from Hazardous Waste to Precious Resource in Obtaining High Value-Added Mesostructured Silica

Mirko Antonio Vacca,[⊥] Claudio Cara,[⊥] Valentina Mameli, Marco Sanna Angotzi, Mariano Andrea Scorciapino, Maria Giorgia Cutrufello, Anna Musinu, Vaclav Tyrpekl, Luca Pala, and Carla Cannas*

Cite This: *ACS Sustainable Chem. Eng.* 2020, 8, 14286−14300

Read Online

ACCESS | Metrics & More | Article Recommendations | Supporting Information

ABSTRACT: In this work, industrial waste hexafluorosilicic acid (H_2SiF_6 or FSA) has been proven to be a low-cost alternative to silicate esters for the synthesis of high-quality MCM-41 (high surface area, high degree of order, narrow pore size distribution, high thermal stability) through a head-to-head comparison between the most common silica precursor, tetraethylorthosilicate (TEOS), and FSA. The effect of different parameters such as temperature, time, hydrothermal treatment, and the presence of ethyl acetate has been explored by studying the textural, structural, and morphological features. On the most promising samples, thermal and hydrothermal stability has been assessed, indicating a higher thermal stability for the FSA-derived sample, due to the thicker walls, and comparable hydrothermal stability. The mother solution treatment has allowed the obtainment of nanostructured fluorite as an additional valuable product and a CTAB-rich ammonia solution for successive synthesis with FSA. Recovery processes for the templating agent entrapped in the MCM-41 mesostructure have also been explored for both FSA- and TEOS-derived samples, showing an easier removal in the case of FSA-MCM-41. Moreover, mesostructured silica derived from FSA has also been proven to be an ideal support to design efficient and regenerable mesostructured iron oxide-based sorbents for H_2S removal from syngas, showing similar performance to that of the corresponding nanocomposite prepared from TEOS.

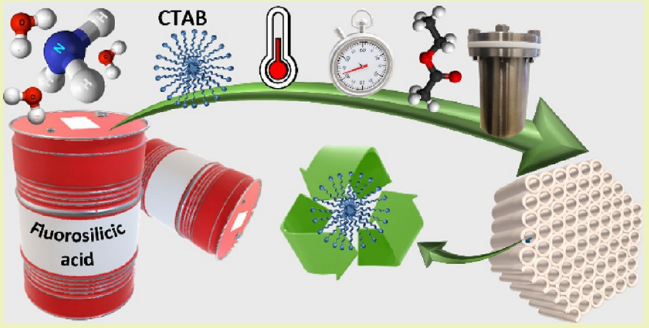

KEYWORDS: *Synthesis, Waste, MCM-41, Hexafluorosilicic acid, Sorbent*

INTRODUCTION

Hexafluorosilicic acid (H_2SiF_6 or FSA) is a hazardous and corrosive byproduct of the production of hydrogen fluoride (HF) and phosphate-containing fertilizers. Large amounts of this industrial waste are produced every year, approximately more than 2 million tons.[1] In the synthetic process of HF, FSA is obtained as a result of the reaction between HF and the inevitable impurities of silica contained in the acid grade fluorspar (CaF_2) used as feedstock: in fact, SiO_2 is one of the major impurities in acid grade fluorspar with a content ranging from 0.5 to 1.5% w/w.[2] The following reactions exemplify how FSA is formed.[3]

$$CaF_2 + H_2SO_4 \rightarrow CaSO_4 + 2HF \quad (1)$$

$$SiO_2{}^* + 4HF \rightarrow SiF_4 + 2H_2O \quad (2)$$

$$3SiF_4 + 2H_2O \rightarrow 2H_2SiF_6 + SiO_2 \quad (3)$$

$$SiF_4 + 2HF \rightarrow H_2SiF_6 \quad (4)$$

The * indicates the compound was found as an impurity in CaF_2.

While eq 1 depicts the standard synthesis of HF from fluorspar and sulfuric acid, eq 2 accounts for the formation of SiF_4, a poisonous gas which in turn generates FSA by reaction with either water in the scrubber eq 3 or HF eq 4. By examining the reaction scheme, it is clear that FSA should be considered not only a major environmental pollutant but also a significant economic burden since it is produced in parasitic reactions, depleting feedstock, and decreasing the yield of the desired product. Moreover, despite few direct applications (*e.g.*, water fluoridation and synthesis of low-density AlF_3), its market share is rather limited and its related compounds, such as fluorosilicates, are generally considered low added-value products with niche applications. For these reasons, disposal at sea upon neutralization is still common practice for FSA

Received: April 29, 2020
Revised: July 3, 2020
Published: August 31, 2020

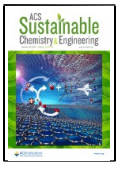

https://dx.doi.org/10.1021/acssuschemeng.0c03218
ACS Sustainable Chem. Eng. 2020, 8, 14286−14300

Table 1. Synthesis Conditions Adopted for the Preparation of the Silica Samples: Reaction Temperature (T), Reaction Time (t), Ethyl Acetate (EA), and Hydrothermal Treatment (Hyd), with the Indication of Their Use (y) or Not (n); Surface Area (S_{BET}), Pore Volume (V_P), DFT-Calculated Pore Diameter ($D_{p(DFT)}$), Wall Thickness (w_t), Lattice Spacing (d_{100}), and Hexagonal Unit Cell Parameter (a_0) for All the Silica Samples[a]

sample	T (°C)	t (h)	EA	Hyd	S_{BET} (m^2 g^{-1})	V_p (cm^3 g^{-1})	$D_{p(DFT)}$ (nm)	w_t (nm)	d_{100} (nm)	a_0 (nm)
TEOS_MCM41 (TEOS_T30_3h_EA)	**30**	3	y	n	1110	0.6	2.6; 3.0	1.2; 0.8	3.3	3.8
FSA_MCM41 (FSA_T30_3h_EA)	**30**	3	y	n	1158	0.6	2.5; 3.1	1.4; 0.8	3.4	3.9
TEOS_T40_3h_EA	**40**	3	y	n	1146	0.7	2.6; 2.9	1.1; 0.8	3.2	3.7
TEOS_T50_3h_EA	**50**	**3**	**y**	**n**	1021	0.7	3.8	0.5	3.7	4.3
TEOS_T60_3h_EA	**60**	3	y	n	1006	0.8	3.3; 3.6	0.9	3.9	4.5
TEOS_T70_3h_EA	**70**	3	y	n	927	0.7	3.0; 3.4	0.9; 0.5	3.9	4.5
FSA_T40_3h_EA	**40**	3	y	n	1169	0.7	2.6; 3.1	1.3; 0.8	3.4	3.9
FSA_T50_3h_EA	**50**	**3**	**y**	**n**	933	0.7	3.4	0.9	3.7	4.3
FSA_T60_3h_EA	**60**	3	y	n	992	0.7	3.5	0.7	3.7	4.3
FSA_T70_3h_EA	**70**	3	y	n	913	0.6	3.7	0.9	4.0	4.6
TEOS_T50_6h_EA	50	**6**	y	n	1005	0.8	3.7	0.7	3.8	4.3
TEOS_T50_18h_EA	50	**18**	y	n	949	0.7	3.7	0.8	3.9	4.5
FSA_T50_6h_EA	50	**6**	y	n	983	0.7	3.4	0.6	3.4	4.0
FSA_T50_18h_EA	50	**18**	y	n	999	0.8	3.6	0.7	3.7	4.3
TEOS_T50_3h_EA_Hyd	50	3	y	**y**	966	0.8	4.0	0.9	4.2	4.9
FSA_T50_3h_EA_Hyd	50	3	y	**y**	817	0.6	3.6	0.9	3.9	4.5
FSA_T50_3h	50	3	**n**	n	1011	0.7	3.4	0.9	3.7	4.3
FSA_T50_3h_ Hyd (MCM41)	50	3	**n**	y	886	0.7	3.6	0.8	3.8	4.4

[a]Relative standard deviation: %RSD (S_{BET}) = 2.1%; %RSD (V_p) = 1.1%; %RSD (D_p) = 1.8%. d_{100} and a_0 were obtained from X-ray diffraction data. For bimodal pore size distributions, two values of $D_{p(DFT)}$ are listed.

derived from fertilizers, especially in those countries with lax environmental regulations, causing detrimental effects to the environment.[4] Nevertheless, FSA should be acknowledged as a valuable and inexpensive source of both fluorine and silicon. As far as fluorine is concerned, hexafluorosilicic acid is thought to be an interesting source of this element in the production of important commodities as an alternative to conventional mineral feedstock (CaF_2). This premise has led scientific research toward the development of promising industrial-scale processes in which FSA might be used in this sense.[1,5,6] Conversely, few examples in which H_2SiF_6 has proved itself to be a suitable precursor in the synthesis of a range of different silicon-containing products (*e.g.*, precipitated silica, zeolites, *etc.*) have been reported in the literature.[7−10] Among these, mesostructured materials stand out as high value-added products with their unique textural properties epitomized by high surface area and pore volume values, regular pore distribution, and a pore diameter within the range 2−50 nm.[11−13] In particular, M41S mesoporous materials have attracted growing interest for their applications in catalysis,[14] chromatography,[15] drug delivery,[16] and environmental remediation.[17−20] MCM-41 is the first and most studied representative of the family featuring regularly arranged cylindrical pores according to a two-dimensional hexagonal symmetry (*P6mm*).[21] The siliceous precursors of these materials are usually alkoxides (namely, TEOS and TMOS, tetraethyl and tetramethylorthosilicate, respectively). However, their considerable cost hinders their large-scale use in the synthesis of mesoporous silica, highlighting the need for more economical alternatives.[8] A number of studies have been devoted to addressing the feasibility of utilizing such alternative silicon sources, which include agricultural waste (i.e., rice husk,[22,23] bagasse,[23] and sedge[24]), industrial byproducts (coal fly ash[25,26] and FSA itself[8,27]), and even e-waste.[28] Among the different waste materials, FSA represents an ideal liquid reactant that can be used without any other pretreatments, for both silicon- and fluoride-based compounds. In the case of the others, the production of MCM-41 involved the obtainment of sodium silicate through severe reaction with NaOH. Furthermore, organic agricultural waste (rice husk, bagasse, and sedge) contains a small amount of silicon, so the production of sodium silicate requires a large amount of feedstock that needs to be treated by calcination. Nevertheless, several papers have been published about the influence of different experimental parameters in the synthesis of MCM-41 from TEOS, but an analogous systematic study with FSA has never been performed. To the best of our knowledge, only one study[8] has been carried out for the synthesis of MCM-41 materials directly from FSA, and another one proposed a synthesis method of MCM-41 starting from the reaction between SiO_2 and HF to produce FSA.[27] The first study was aimed at developing novel mesostructured xSi/Ti-MCM-41 materials from FSA industrial waste and tested them as epoxidation catalysts. In the second work, the authors focused on Al- and Ti-containing silica-based mesoporous materials with different Al/Si and Ti/Si ratios. In both papers, the authors mainly focused on the mixed-silica materials, and a pure silica sample was used only as a reference material.

In the present work, a head-to-head comparison of MCM-41 synthesized by using either TEOS or FSA as precursors is presented in order to assess the best experimental conditions for the synthesis of high-quality MCM-41 from FSA, in terms of temperature, time, hydrothermal treatment, and the presence of ethyl acetate. On the most promising samples derived from the two precursors, thermal and hydrothermal stability is also studied. To save the templating agent, the most expensive reagent used in the synthesis, recovery strategies for CTAB-rich ammonia solution and CTAB molecules from the mesopores are reported in the view of realizing a high atom-efficiency process. A 10% w/w Fe_2O_3-containing mesoporous material is also prepared via the so-called two-solvent impregnation technique,[29] with the application as a sorbent

https://dx.doi.org/10.1021/acssuschemeng.0c03218
ACS Sustainable Chem. Eng. 2020, 8, 14286−14300

for H_2S removal from sour syngas, whose performance was then compared with that of a similar sorbent derived from TEOS.

EXPERIMENTAL SECTION

Chemicals. The following chemicals were of analytical grade and used as received without further purification: hexadecyltrimethylammonium bromide (Sigma-Aldrich, CTAB, 98% w/w), ethyl acetate (Sigma-Aldrich, EA, 99.8% w/w), ammonia solution (Sigma-Aldrich, 30% w/w), tetraethyl orthosilicate (Sigma-Aldrich, TEOS, 98% w/w), ethanol (Sigma-Aldrich, EtOH, 96% v/v), calcium hydroxide (Ca(OH)2, Carlo Erba, 95%w/w). FSA solution (Honeyweel, 34% w/w) was diluted to 23.8% w/w with double-distilled water, and the concentration determined by a titration method according to ref 30. Double-distilled water was used throughout the experiments.

MCM-41 Preparation from TEOS and FSA. MCM-41 was synthesized according to an opportunely modified synthetic procedure retrieved from the literature.[20] A total of 1 g of CTAB was dissolved in 200 mL of double-distilled water under mild stirring (300 rpm) for 1 h at 30 °C. Then, 21 mL of ammonia solution was added. At this stage, the temperature was kept at 30 °C or increased to 40, 50, 60, and 70 °C. Once the desired temperature was reached, 3.85 mL of EA was added, and the reacting mixture was kept for 10 min at the same stirring rate and temperature. The stirring rate was then increased up to 600 rpm and 3.79 mL of TEOS (or 9.00 g of FSA solution) was injected all at once into the reaction mixture. The molar ratios Si (TEOS or FSA)/NH_3/CTAB/EA/H_2O in the reaction mixtures were 6:120:1:14:4400. After 5 min, the resulting opalescent dispersion was allowed to react for 3, 6, or 18 h under constant stirring at 300 rpm. The product was then separated by centrifugation (4500 rpm for 5 min), washed three times with 65 mL of a 1:1 H_2O/EtOH mixture, dried overnight at 60 °C, and eventually calcined under static air at 550 °C for 4 h (heating rate 2 °C min^{-1}) to remove the templating agent. Some reactions were also performed without the addition of EA to investigate its possible effect on morphology. *T*, *t*, and EA were used in the label of the samples to provide information about the temperature, time, and the presence of EA, while AS was added for the as-synthesized sample without any further treatment beyond the washing and centrifugation cycles. An ancillary static hydrothermal treatment was carried out in some samples using a 330 cm^3 Teflon-lined autoclave for 18 h at 100 °C immediately after the conclusion of the reaction. The label "Hyd" was added to the name of the sample when the hydrothermal step was performed. Once the proper temperature for both the precursors was defined, the effect of time was then screened, and the effects of hydrothermal treatment and EA were investigated. In the samples synthesized from FSA and washed three times, the fluorine content was verified by Wavelength Dispersive X-ray Fluorescence (WD-XRF) analyses (Bruker S8 Tiger). In all the cases, it was below 0.5% w/w. Further washing cycles were also attempted, proving that fluorite can be completely removed through a thorough washing procedure. The yields in SiO_2 were between 88 and 93% for both FSA and TEOS, regardless of temperature, time, and other experimental conditions.

A flowchart of the reaction sets performed for the head-to-head comparison is depicted in Figure S1 with the experimental conditions examined and summarized in Table 1.

Fe_2O_3-Based Nanocomposite Preparation. The synthesis of the Fe_2O_3-based nanocomposite was performed via the so-called two-solvent incipient impregnation technique.[29,31] A total of 0.250 g of the bare calcined MCM41 support (also labeled FSA_T50_3h_ Hyd, Table 1) was dried at 120 °C for 48 h and then suspended in 20 mL of *n*-hexane. The mixture was then stirred at 250 rpm for 4 h. Therefore, a suitable amount of impregnating aqueous solution of $Fe(NO_3)_3{\cdot}9H_2O$ was carefully added dropwise. The dispensed amount of impregnating solution was calculated by taking into account the pore volume value obtained from N_2-physisorption measurements. After 2 h, the *n*-hexane was evaporated by increasing the temperature to 80 °C. The resulting solid was kept in an oven at 80 °C overnight and then calcined at 500 °C for 2 h (heating rate 2 °C min^{-1}) to decompose the nitrate precursor and obtain the corresponding nanocomposite (10Fe_MCM41).

Recovery of the Templating Agent. The as-synthesized bare support MCM41_AS (FSA_T50_3h_Hyd, Table 1) was prepared to recover the templating agent by extraction with two different solvents: ethanol or water. The procedure was retrieved in the literature[32] and adapted for the present work. One portion of 750 mg was placed into a cellulose extraction thimble and carefully laid into a Soxhlet apparatus by using a Dimroth condenser connected to a chiller set at 5 °C. The 500 cm^3 flask of the apparatus was filled with 200 mL of either EtOH (96.4% w/w) or water and heated at 110 °C for 48 h. Regular sampling (at 15 min, 30 min, 1, 3, 6, and 48 h) was performed to assess the progress of the extraction via Fourier transform infrared FT-IR spectroscopy (Figure S7). After 48 h, the product was recovered, and a portion was calcinated at 550 °C for 4 h (heating rate, 2 °C min^{-1}) to assess the porous structure stability of the sample after extraction. The extracting solution was then evaporated to recover the templating agent. The samples were labeled as MCM41_ExE and MCM41_ExW for MCM41 extracted by either ethanol or water, respectively.

The recovery of the templating agent was also attempted in the case of the TEOS_T50_3h_Hyd sample by extraction with ethanol and ethanol/HCl solution. This latter was prepared by adding 2.8 g of 37% w/w HCl to 200 cm^3.[33]

Thermal and Hydrothermal Stability Assessment. The thermal and hydrothermal stability were studied for the samples TEOS_T50_3h_Hyd and FSA_T50_3h_Hyd, upon calcination at 550 °C for 4 h (heating rate, 2 °C min^{-1}). To assess thermal stability, four aliquots of 150 mg for each sample were placed into a muffle oven, heated with a heating rate of 2 °C min^{-1} at 650 °C, 750 °C, 900 °C, and 950 °C and kept for 1 h. Hydrothermal stability was assessed in water by following the procedure described in the literature:[34] 150 mg of the calcined sample was dispersed in 10 mL of double-distilled water in a three-neck round-bottom flask equipped with an Allihn condenser at 100 °C for 4 h under magnetic stirring. The samples were then recovered by centrifugation at 4500 rpm for 5 min and dried.

Desulphidation Activity and Regenerability of the Sorbents. To determine the desulphidation capacities, 100 mg of composite was placed on a quartz wool bed (50 mg) in a vertical quartz tubular reactor, coaxially located in an electrical furnace. Before desulphidation, a pretreatment at 300 °C for 30 min under helium flow was performed to remove air and water from the sorbent and the reactor. Then, a sour syngas atmosphere containing 1.52% v/v (15200 ppm) of H_2S, 24.88% v/v of CO, and 14.84% v/v of H_2 in N_2 was fed to the reactor (inlet flow 20 cm^3 min^{-1}) and the H_2S content in the outlet flow during the adsorption test was monitored by a quadrupole mass spectrometer (Thermo Electron Corporation). At the same time, H_2O, CO, H_2, and CO_2 signals were also monitored. When the outlet concentration of H_2S reached 15200 ppm, the measure was stopped and the system was purged in flowing helium (20 cm^3 min^{-1}) for 1 h. The amount of sulfur retained per unit mass of sorbent (sulfur retention capacity (SRC)) was determined when the outlet H_2S concentration attained 100 ppm by the formula SRC = $(F_sB_t)/W$, where F_s is the mass flow rate of sulfur (mg of S s^{-1}), B_t is the breakthrough time (s), and *W* is the sorbent weight (g), referring to the composite. The sulfur retention capacity of the sorbents was obtained as the difference between the B_t value of the composite and the B_t value of the bare support. The error on the SRC values was estimated at 2 mg_S $g_{sorbent}^{-1}$ by carrying out several sulphidation cycles on fresh portions of the commercial sorbent $Katalko_{JM}$ 32-5. The regeneration process was performed on a Thermoquest 1100 TPD/R/O apparatus equipped with a thermal conductivity detector (TCD) and a quadrupole mass spectrometer (QMS) for monitoring SO_2, CO_2, and O_2 signals. The composite was heated under an air flow (20 cm^3 min^{-1}) up to 500 °C (heating rate, 10 °C min^{-1}), and the temperature was kept constant for 3 h. To identify the samples after different cycles of sulphidation and regeneration processes, a letter R

https://dx.doi.org/10.1021/acssuschemeng.0c03218
ACS Sustainable Chem. Eng. 2020, 8, 14286−14300

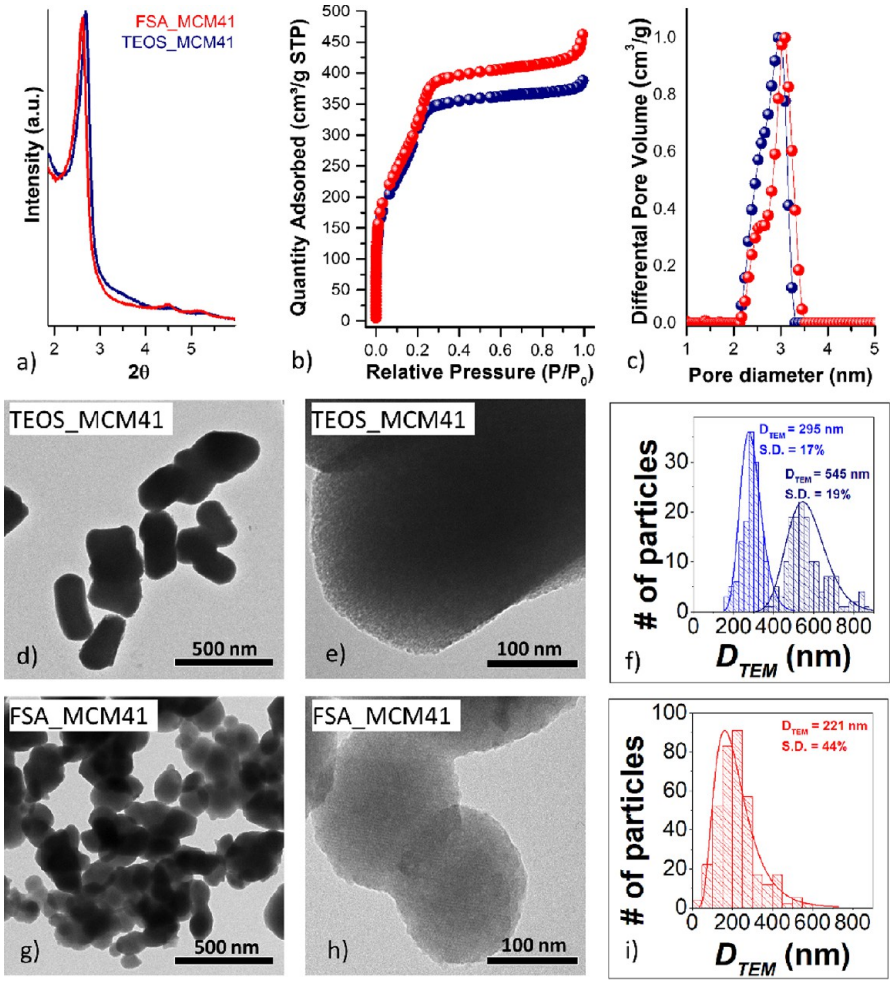

Figure 1. SA-XRD patterns (a), N_2-physisorption isotherms (b), DFT-calculated pore size distributions (c), TEM micrographs (d–e and g–h) and particle size distribution calculated by TEM with about 150 and 300 particles in the case of TEOS_MCM41 and FSA_MCM41, respectively (f, i) of the samples TEOS_MCM41 (d–f) and FSA_MCM41 (g–i).

and a number (denoting successive cycles) were added in the sample name.

Characterization. Small-angle (SA, $2\theta = 0.8°–6°$) and wide-angle (WA, $2\theta = 10–70°$) X-ray diffraction patterns were recorded on a Seifert X3000 instrument with a $\theta–\theta$ geometry featuring a Cu Kα anode ($\lambda = 1.5406$ Å). The lattice parameter was calculated using the equation $a_0 = (2d_{100})/\sqrt{3}$. SA-XRD measurements on the samples presented in the study of the Thermal and Hydrothermal Stability section were conducted by using the same amount of sample (1.5 g), in order to correlate the counts at the detector with the mesoporous order as a function of the treatment temperature.

Textural analyses were performed on a Micromeritics ASAP 2020 system by determining the nitrogen adsorption–desorption isotherms at −196 °C. Prior to analyses, the samples were heated for 12 h under a vacuum at 250 °C (heating rate, 1 °C min^{-1}). The Brunauer–Emmett–Teller (BET) specific surface area (S_{BET}) was calculated from the adsorption data in the P/P_0 range 0.05–0.17.[35] Total pore volume (V_p) was calculated at $P/P_0 = 0.875$, while mean pore diameter was determined by applying both the density functional theory (DFT) model (assuming N_2 as the adsorptive gas, cylindrical pores, and an oxide-based surface) on the isotherm adsorption branch and the Barrett–Joyner–Halenda (BJH) model to the isotherm desorption branch (Figure S2). Wall thickness (w_t) was calculated as the difference between the lattice parameter (a_0) and the pore diameter obtained by the DFT model ($D_{p(DFT)}$). The samples treated to assess thermal and hydrothermal stability (study of the Thermal and Hydrothermal Stability section) were characterized by using a Sorptomatic 1990 System (Fisons Instruments) that allows a determination of the pore size distribution by the BJH method.

Transmission electron microscopy (TEM) images were obtained on a JEOL JEM 1400-PLUS microscope operating at an accelerating voltage of 120 kV. High-resolution TEM (HRTEM) images were carried out using a JEOL JEM 2010 UHR microscope equipped with a 794 slow-scan CCD camera operating at 200 kV. Finely ground powders of the samples were first dispersed in ethanol and sonicated. The resulting suspensions were dropped onto 200 mesh carbon-coated copper grids.

FT-IR spectra were collected by using a Bruker Equinox 55 spectrophotometer in the range 400–4000 cm^{-1} with the samples being analyzed after dispersing them in KBr.

Thermogravimetric analysis (TGA) curves were obtained through a PerkinElmer STA 6000. The temperature range investigated was 25–850 °C, while the heating rate was set at 10 °C min^{-1}. Measurements were performed under a 40 mL min^{-1} flow of O_2.

The fluoride concentration (w/w) was determined through a Metrohm 781 pH/Ion Meter with a Metrohm fluoride ion selective electrode coupled with Metrohm reference electrode Ag/AgCl. A proper amount of sample was weighted and diluted to 25 mL and added at 25 mL of total ionic strength adjusting buffer solution (TISAB). The resulting solution was finally analyzed.

The ^{57}Fe Mössbauer spectrum was recorded at room temperature (RT) on a Wissel spectrometer calibrated with a foil of α-Fe as the reference standard and the data elaborated with the software NORMOS.

https://dx.doi.org/10.1021/acssuschemeng.0c03218
ACS Sustainable Chem. Eng. 2020, 8, 14286–14300

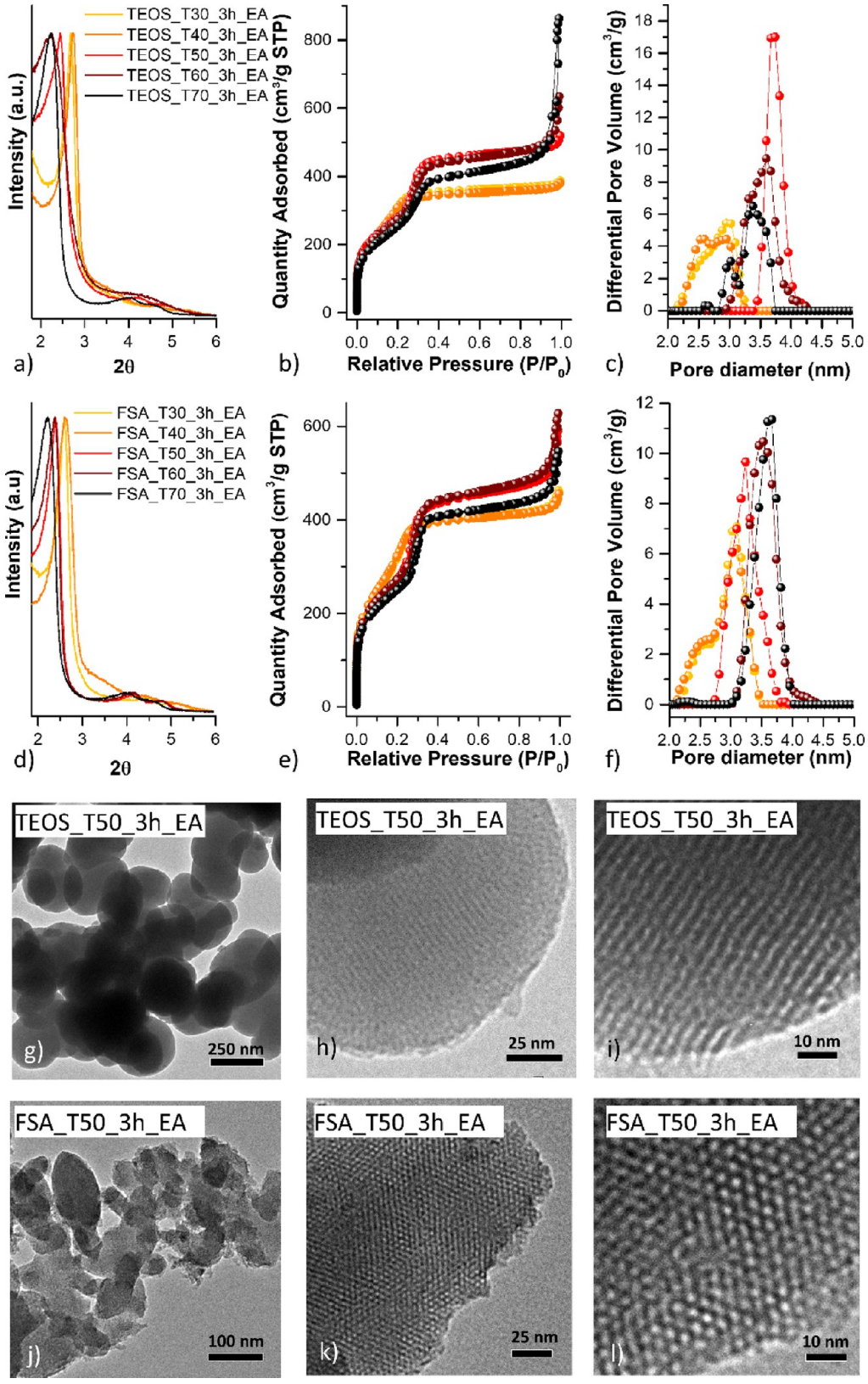

Figure 2. SA-XRD patterns (a, d), N_2-physisorption isotherms (b, e), and DFT-calculated pore size distributions (c, f) of synthesized MCM-41 at different temperatures using either TEOS (a–c) or FSA (d–f). TEM micrographs of the samples synthesized at 50 °C: TEOS_T50_3h_EA (g–i), FSA_T50_3h_EA (j–l).

DC magnetic properties were studied with a Quantum Design PPMS Dynacool (H_{max} = 90 kOe) by using the VSM module. The field dependence of the magnetization was studied at 5 K between −90 kOe and +90 kOe. The dependence on temperature of the magnetization was studied by using zero-field-cooled (ZFC) and field-cooled (FC) protocols: the sample was cooled down from 300 to 2 K

https://dx.doi.org/10.1021/acssuschemeng.0c03218
ACS Sustainable Chem. Eng. 2020, 8, 14286−14300

in zero magnetic field; then, the curve was recorded under a static magnetic field of 250 Oe. M_{ZFC} was measured during the warm-up from 2 to 300 K, whereas M_{FC} was recorded both during cooling and warm-up.

For ^{29}Si-MAS solid-state NMR analysis, the samples MCM41_Ref and MCM41 (FSA_T50_3h_Hyd) were packed in a 2.5 mm diameter MAS rotor (internal volume 14 μL). Spectra were recorded at RT on an Avance III HD spectrometer (Bruker, Billerica, MA, USA) operating at a ^{1}H frequency of 600 MHz (^{29}Si: 119.229 MHz). Octakis(trimethylsiloxy)silsesquioxane (Q8M8) was used as an external reference to calibrate the chemical shift scale, by setting its high frequency ^{29}Si resonance at +12.6 ppm. ^{29}Si-MAS spectra were acquired at a 10 kHz spinning rate and using a 1.8 μs pulse (30°), 30 s delay time, 6 ms acquisition time, and a spectral width of 50 kHz for 1700 transients. Spectra processing and analysis, including deconvolution, were carried out with the software iNMR v.5.4.6 (2015, Mestrelab Research).

RESULTS AND DISCUSSION

Synthesis of MCM-41 from FSA. Starting from a well-established procedure to obtain MCM-41 from TEOS,[20] a tentative synthesis in the same experimental conditions was performed by replacing TEOS with FSA (TEOS_MCM41 and FSA_MCM41). Surprisingly, the two precursors gave very similar results in terms of porous structure, surface area, pore volume, pore diameter, and pore size distribution (Table 1, Figure 1), although the reactions involved are rather different. An acid−base reaction (eq 5), in which ammonia is a stoichiometric reactant, followed by a second reaction producing silica (eq 6), occurs in the case of FSA. Hydrolysis (eq 7) and condensation reactions (eq 8 with water formation and eq 9 with ethanol formation) are involved in the case of TEOS, with ammonia acting as a mere catalyst. From eq 6, the reaction with FSA yields an aqueous solution containing NH_4F. This solution may be employed to recover ammonia in several ways: in the production of both HF,[36] a valuable commodity consumed by the same parasitic reactions that generate FSA, and CaF_2[6,37] with important economic and environmental advantages. The abatement of fluoride ions in the aqueous solution containing NH_4F was attemped by adding a stoichiometric amount of $Ca(OH)_2$ and heating the resulting solution at 90 °C. The obtained solid was separated from the solution by filtration.[6] Both the solid and the liquid phases were characterized. The WA-XRD analysis (Figure S3 upper part) of the solid showed peaks ascribable to fluorite, in the form of ∼20 nm crystallites, whereas the absence of C−H stretching in the FTIR spectra (Figure S3 bottom part) proved the absence of CTAB adsorbed on the solid. The concentration of fluoride in the supernatant obtained after separation of MCM-41 silica and after CaF_2 precipitation dropped from 0.89% w/w to 0.04% w/w, proving the obtainment of a basic solution poor in fluoride but rich in CTAB that, in principle, might be recycled to obtain MCM-41 by the addition of FSA.

$$H_2SiF_6 + 2NH_4OH \rightarrow (NH_4)_2SiF_6 + 2H_2O \quad (5)$$

$$(NH_4)_2SiF_6 + 4NH_4OH \rightarrow SiO_2 + 6NH_4F + 2H_2O \quad (6)$$

$$Si(OEt)_4 + H_2O \rightarrow Si(OEt)_3OH + EtOH \quad (7)$$

$$2(OEt)_3SiOH \rightarrow (OEt)_3Si - O - Si(OEt)_3 + H_2O \quad (8)$$

$$(OEt)_3SiOH + Si(OEt)_4 \rightarrow (OEt)_3Si - O - Si(OEt)_3 + EtOH \quad (9)$$

The SA-XRD pattern of the material derived from FSA shows the formation of a highly ordered hexagonal pore structure, typical of MCM-41, such as the one derived from TEOS (Figure 1a). The N_2-physisorption isotherms reported in Figure 1b fit well into the definition of an IVB isotherm, which is typical of mesoporous materials such as MCM-41. The mesoporous contribution is confirmed by the distinct step in the range 0.2−0.3 P/P_0 related to the capillary condensation phenomenon.[38] A comparison between BJH- and DFT-calculated pore size distribution is reported in Figure S2, although the DFT model was preferred in this case, allowing more accurate values of pore size in the range of 2−5 nm (Figure 1c, Table 1).

The similar textural properties are, however, accompanied by different morphological features. By examining TEM micrographs at low magnification for the sample TEOS_MCM41 (Figure 1d), it is possible to observe regular submicrometric particles with cylindrical shapes (about 300 nm widthwise and about 550 nm lengthwise, Figure 1f). Rounded, hexagonal, or seed-shaped submicrometric particles having an average particle size of about 220 nm with a broad particle size distribution are observed when FSA is used (Figure 1g and i). High magnification images confirm the well-defined mesoporous order in both samples (Figure 1e and h). Interestingly, in the FSA-derived samples, it is possible to clearly observe that the mesoporous order extends to the outer layers of the material.

Effect of the Synthetic Parameters. MCM-41 from TEOS and the effect of different parameters such as temperature, reaction time, hydrothermal treatment, pH, ratio between TEOS and CTAB, and EA have been widely studied.[39,40] Here, we propose a systematic study on MCM-41 from FSA, changing the different synthetic parameters as well as a comparison with TEOS-derived samples.

Effect of Temperature. When choosing the temperature for a soft-template synthesis, two features of the templating agent are deemed to have a pivotal role. The first is the critical micellar temperature (CMT), also referred to as Krafft temperature, which is the minimum temperature for a given surfactant to form micelles. The second parameter is the cloud point (CP), defined as the temperature at which phase separation of the solvent−surfactant mixture occurs.[39] CMT values for cationic surfactants such as CTAB are usually close to room temperature (20−25 °C),[39] and therefore, synthesis temperatures between 30 and 70 °C were adopted.

As shown in Figure 2, SA-XRD patterns reveal the mesostructured nature of the samples synthesized either with TEOS or FSA at the selected temperatures: all the patterns feature the three typical peaks of highly ordered hexagonal structures, referred to as (100), (110), and (200). Concerning MCM-41 deriving from TEOS, the results indicate that the samples obtained at 30 and 40 °C show similar patterns with a narrow (100) peak. By increasing the temperature, the peaks move toward lower angles with the co-occurring broadening of the (100) peak. N_2-physisorption analyses confirm the similarities between the samples synthesized at 30 and 40 °C with comparable values of specific surface area (1110 $m^2\ g^{-1}$, 1146 $m^2\ g^{-1}$), pore volume (0.6 $cm^3\ g^{-1}$, 0.7 $cm^3\ g^{-1}$), and a bimodal pore size distribution (Table 1). At 50 °C, unimodal

https://dx.doi.org/10.1021/acssuschemeng.0c03218
ACS Sustainable Chem. Eng. 2020, 8, 14286−14300

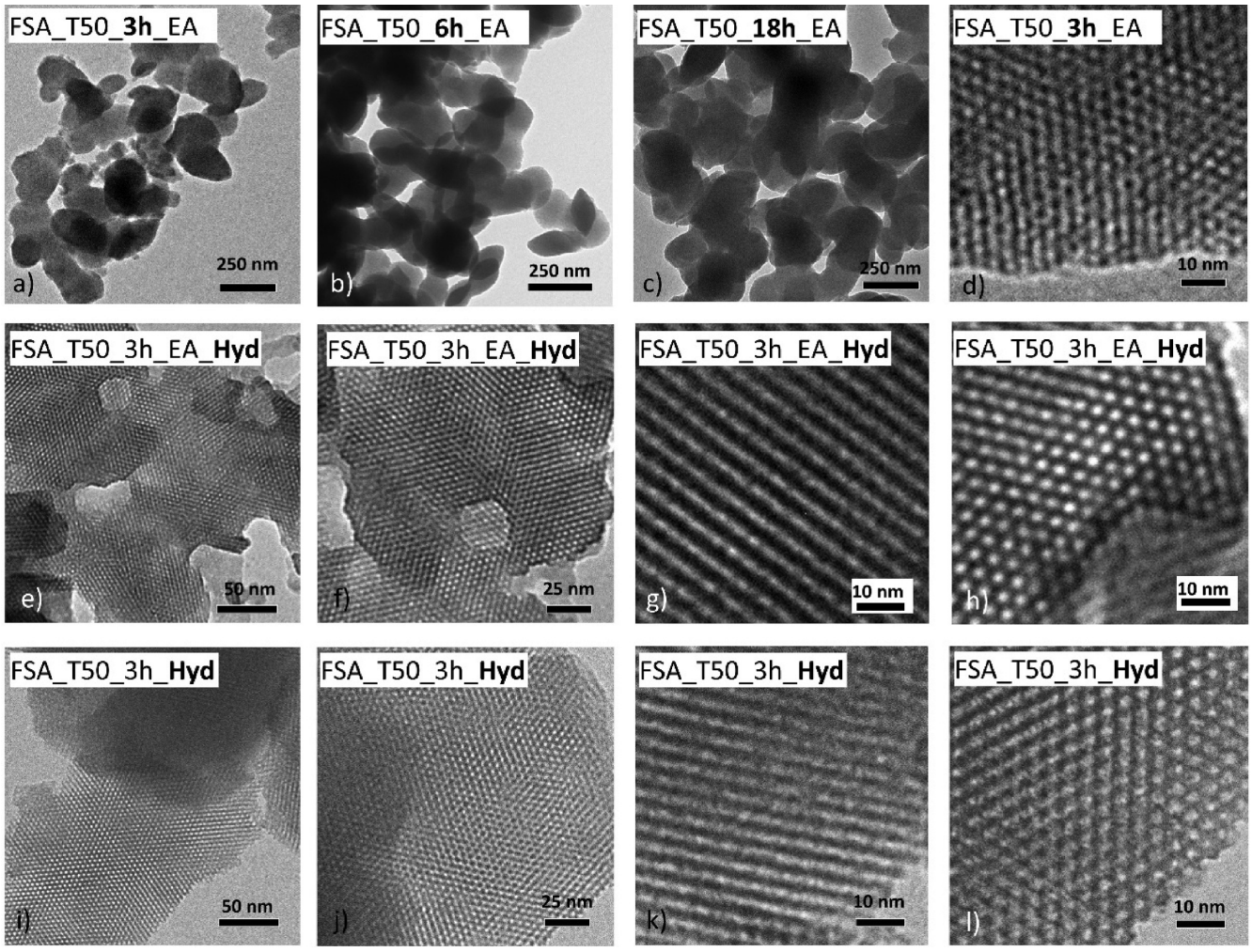

Figure 3. TEM micrographs of MCM-41-derived from FSA synthesized at different reaction times: FSA_T50_3h_EA (a, d), FSA_T50_6h_EA (b), FSA_T50_18h_EA (c). TEM images at different magnifications of the samples subjected to the hydrothermal treatment in the presence of ethyl acetate (EA), FSA_T50_3h_EA_Hyd (e–h), and in its absence, FSA_T50_3h_Hyd (i–l).

pore size distribution was achieved along with an increase of the pore diameter ($D_{P(DFT)}$ = 3.8 nm), and then, at 60 and 70 °C, a bimodal pore size distribution was observed again. The sample obtained at 70 °C distinguished itself by a steep increase in the isotherm curve at high values of P/P_0 (close to 1), associated with interparticle porosity.

SA-XRD patterns of the samples obtained from FSA (Figure 2d) show a similar behavior: by increasing the temperature, the peaks move toward lower angles with a slight broadening of the (100) peak and, for the samples synthesized at 50 °C, 60 °C, and 70 °C, the (110) and (200) peaks are more discernible. Textural properties were affected in a similar way as TEOS-derived samples: at 30 and 40 °C, the highest specific surface areas (1158 m^2 g^{-1}, 1169 m^2 g^{-1}), smaller pore diameters (2.6–3.1 nm), and bimodal pore size distributions were observed, while from 50 to 70 °C a monomodal and narrow pore size distribution were revealed. Therefore, 50 °C was chosen as the optimal temperature at which to carry out the time-dependent experiments, being the minimum temperature at which a narrow unimodal pore size distribution was achieved in both precursors. The general trend of d_{100}, a_0, and surface area values as a function of the temperature might be justified by the expected swelling of the surfactant agents with increasing the temperature, due to the increase in the pore size and, as a consequence, in the pore volume and the corresponding decrease in the surface area.

Figure 2g and j depict TEM images for the comparison between TEOS- and FSA-derived materials at the same temperature (50 °C) to verify the effect on their morphology according to the different precursor employed. In the case of TEOS (TEOS_50_3h_EA), it is possible to verify that the increase of the temperature from 30 to 50 °C affected the particle shape from cylindrical to spheroidal, and the size decreased to about 200–250 nm (Figures 1d–f and 2g). On the contrary, no significant changes in the shape and size of the particles were observed for the FSA-derived counterpart (FSA_50_3h_EA), still showing submicrometric particles of different shapes of about 200 nm (Figure 1g–i and Figure 2j). The images at high magnification confirm the high degree of order in the porous system for both the samples (Figure 2h,i and k,l).

Effect of Time. By comparing the textural properties of the mesoporous siliceous materials from TEOS and FSA at different reaction times (3, 6, and 18 h) but keeping the same temperature determined in the previous set of experiments (T = 50 °C), no remarkable effects were detected on both samples (Figure S4), even if slight differences in the surface area with opposite trends can be revealed for the two

https://dx.doi.org/10.1021/acssuschemeng.0c03218
ACS Sustainable Chem. Eng. 2020, 8, 14286–14300

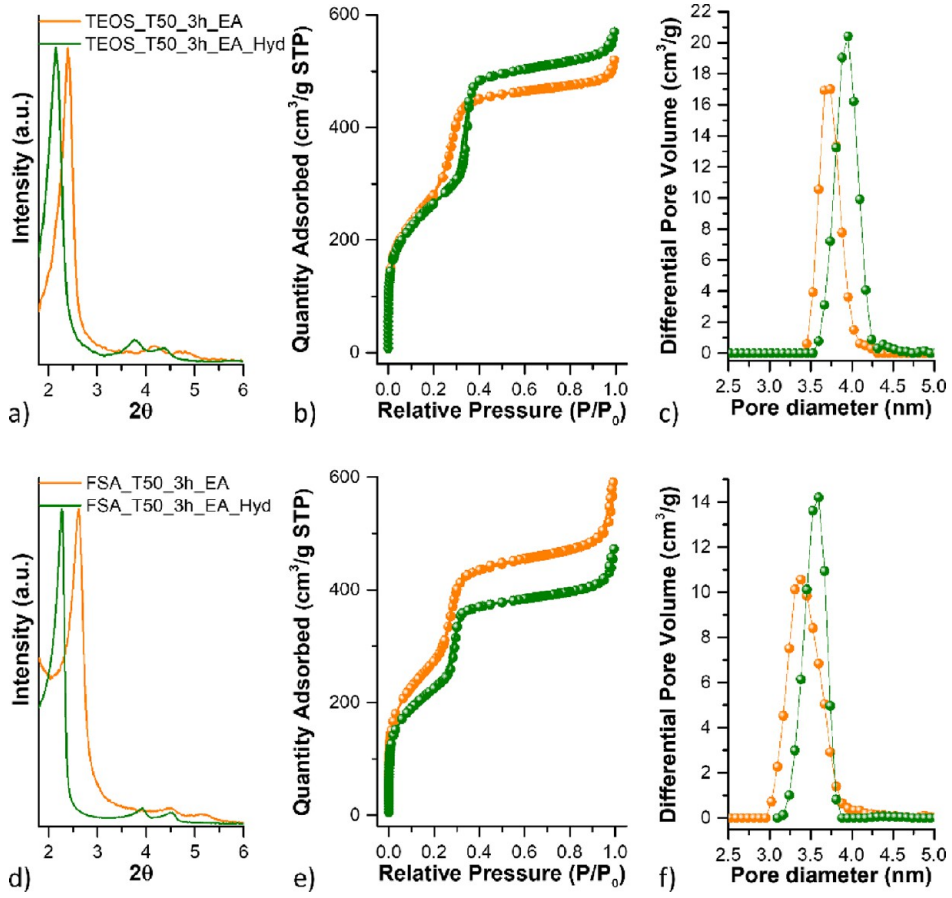

Figure 4. SA-XRD patterns (a, d), N_2-physisorption isotherms (b, e), and DFT-calculated pore size distributions (c, f) of MCM-41 synthesized in the presence of ethyl acetate (EA), with and without hydrothermal treatment (Hyd).

sets (Table 1). TEM micrographs at low magnification performed on FSA-derived samples (Figure 3a–c) show an increase in the mean dimensions of the irregularly shaped particles from about 200 nm up to about 500 nm for a reaction time of 18 h (FSA_T50_18h_EA). Eventually, 3 h was chosen as the optimal reaction time for its convenience, especially considering possible applications in industrial settings.

Meléndez-Ortiz et al.[40] also investigated the effect of time in the synthesis of MCM-41 on a different reaction mixture that included TEOS as a Si precursor and EtOH as the solvent. When synthesis time was increased, peak positions shifted at higher 2θ values, with the associated reduction in d_{100} and a_0 values. In our case, when using TEOS as the precursor but water as the only solvent, only a very slight and progressive shift of the SA-XRD peaks toward lower values of 2θ and the related increase of d_{100} and a_0 were observed (Table 1).

Effect of the Hydrothermal Treatment. Generally, to strengthen the porous structure, an additional hydrothermal treatment is applied during the synthesis of the mesostructured silica. In the case of SBA-15,[41] this further treatment induces a decrease in the microporous contribution, while for MCM-41 a small increase in the pore size and wall thickness, as well as an improvement in the mesoporous order, have been reported.[19] Moving in this direction, the synthetic strategy (50 °C, 3 h) was modified by adding a hydrothermal treatment at 100 °C for 18 h.[42] As shown in Figure 4 and Table 1, in both TEOS- and FSA-derived samples, the ancillary hydrothermal treatment brought about a better definition of the (110) and (200) peaks, an indication of an improved order in the mesoporous structure, along with wider pores (+0.2 nm for both TEOS and FSA) with a corresponding decrease in the specific surface area (from 1021 to 966 $m^2\ g^{-1}$ for TEOS-derived MCM-41, and from 933 to 817 $m^2\ g^{-1}$ for FSA-derived MCM-41).

TEOS_T50_3h_EA_Hyd features thicker pore walls compared with the untreated sample, in agreement with the literature.[19] For the FSA-derived MCM-41 sample (FSA_T50_3h_EA_Hyd), wall thickness resulted in being unaffected by the hydrothermal treatment while pore diameter increased (from 3.4 to 3.6 nm) and pore size distribution became narrower. The hydrothermal treatment also influences the morphology of the particles in terms of size and shape: the FSA_T50_3h_EA_Hyd sample shows particles with irregular shapes and large dimensions in the 300–400 nm range (Figure 3e–h, Figure S5). This batch of experiments reveals the efficiency of hydrothermal treatment in improving the order of pores of both TEOS- and FSA-derived silicas.

Effect of Ethyl Acetate. In all the syntheses proposed so far, EA was employed. The effect of EA as a growth-inhibiting agent is known in the literature in the case of TEOS-derived silica, which is mainly due to the decrease in pH upon its hydrolysis, leading to the formation of acetic acid.[43] However, the effect of EA on FSA-derived silica synthesis is expected to be different due to its acidic nature, but it has never been an object of study. For this reason, two experiments were carried out to verify the possible changes in the textural and morphological properties of FSA-derived silicas in the absence of EA, with (FSA_T50_3h_Hyd) and without (FSA_T50_3h) a hydrothermal treatment. The two resulting samples were

https://dx.doi.org/10.1021/acssuschemeng.0c03218
ACS Sustainable Chem. Eng. 2020, 8, 14286–14300

Table 2. Surface Area (S_{BET}), Pore Volume (V_p), DFT-Calculated Pore Diameter ($D_{p(DFT)}$), Wall Thickness (w_t), Lattice Spacing (d_{100}), Hexagonal Unit Cell Parameter (a_0) of the Samples Involved in the Extraction of CTAB with Solvent and MCM41 As Reference. The treatment and activation conditions are also listed. The activation of the samples MCM41_ExE and MCM41_ExW was performed at 110 °C, the same temperature at which the extraction had been performed[a]

sample	treatment	activation for N_2-Physis.	S_{BET} (m^2 g^{-1})	V_p (cm^3 g^{-1})	$D_{p(DFT)}$ (nm)	w_t (nm)	d_{100} (nm)	a_0 (nm)
MCM41	calcination at 550 °C	250 °C 12 h	886	0.7	3.6	0.8	3.8	4.4
MCM41_ExE	extraction with EtOH	110 °C 12 h	850	0.7	3.7	1.0	4.1	4.7
MCM41_ExE_C	extraction with EtOH and calcined at 550 °C	250 °C 12 h	356	0.4				
MCM41_ExW	extracted with water	110 °C 12 h	247	0.7				

[a]Relative standard deviation: %RSD (S_{BET}) = 2.1%; %RSD (V_p) = 1.1%; %RSD (D_p) = 1.8%. d_{100} and a_0 were obtained from X-ray diffraction data.

compared with FSA_T50_3h_EA_Hyd and FSA_T50_3h_EA. As expected, EA does not cause any remarkable effect on silica, as confirmed by SA-XRD patterns, N_2-physisorption isotherms (let alone the effects of hydrothermal treatment), and pore size distribution in both the hydrothermally treated and untreated samples (Figure S6 and Table 1). TEM images ultimately confirm these findings, showing irregularly shaped particles in both the samples, with dimensions in the range of 300−400 nm (Figure 3i−l for the sample FSA_T50_3h_Hyd, Figure S5).

CTAB Recovery. Aiming to make the use of MCM-41-based materials from FSA competitive on large-scale market production, the possibility of recovering the templating agent from mesopores, besides ammonia and fluorine, is worth considering. In fact, calcination entails the impossibility of recovering the templating agent of M41S mesoporous materials.[44,45] In this view, a further reduction of the costs and a high atom-efficiency process utilizing FSA might be obtained by extracting CTAB. Here, attempts were carried out with either ethanol or water. The extraction was performed on an *ad hoc* sample (prepared under the same conditions of FSA_T50_3h_Hyd but without calcination treatment, labeled MCM41_AS) with a Soxhlet apparatus, sampling at 15 min, 30 min, and 1, 3, 6, and 48 h, and monitored by FT-IR (Figure S7a,b). The almost complete removal of CTAB from MCM-41 was achieved already after 1 h of extraction with ethanol (Figure S7a), while a similar result was obtained after 48 h in the case of water extraction (Figure S7b). These results were confirmed by thermogravimetric analysis (Figure S7c). The efficiency of the extraction with ethanol (MCM41_ExE) is confirmed by the presence of a single step of weight loss at about 100 °C (9%) ascribable to the adsorbed water; to the contrary, the sample MCM41_ExW, let alone the first weight loss of about 3% related to water, shows a second step at 240 °C of about 9% due to the CTAB, still present after 48 h of extraction.

Besides the ability of the solvents to remove the templating agent, another crucial issue is the preservation of the preformed mesostructure after the extraction phase. To study this aspect, N_2-physisorption analyses were performed on the samples extracted after 48 h both in ethanol (MCM41_ExE) and in water (MCM41_ExW) and compared with FSA_T50_3h_Hyd (labeled for simplicity MCM41). The textural properties of these samples are reported in Table 2. The mesostructure was preserved in the sample MCM41_ExE, as confirmed by the N_2-physisorption isotherm (Figure 5a) and the pore size distribution (Figure 5b), that result in being almost superimposable with that of the sample MCM41. To verify the thermal stability of the mesostructure, MCM41_ExE

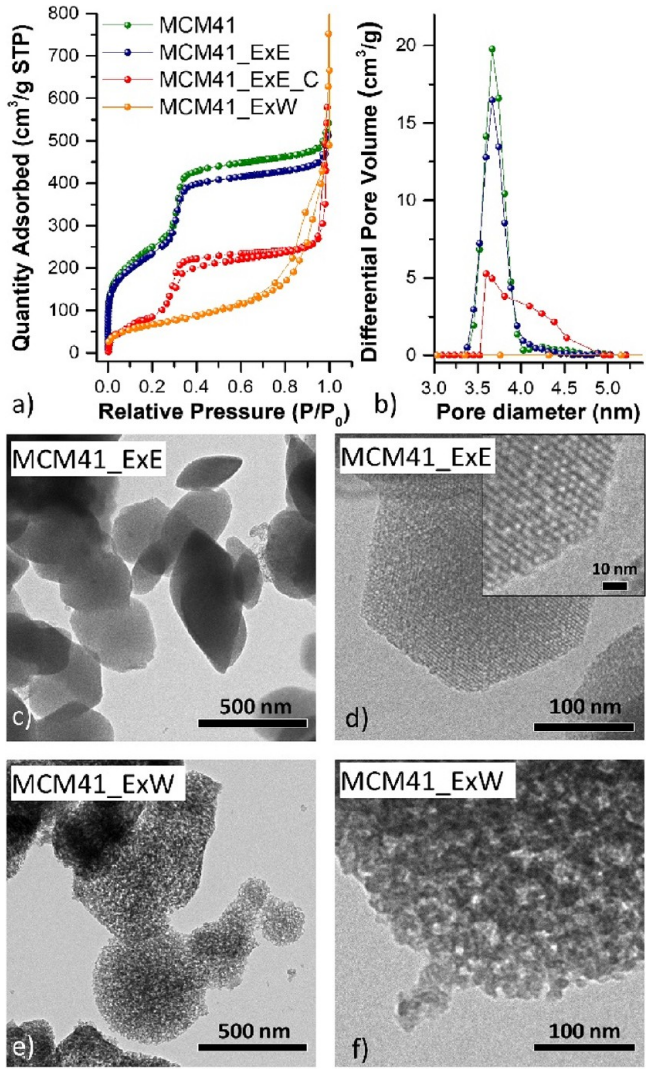

Figure 5. N_2-physisorption isotherms (a) and DFT-calculated pore size distributions (b) of the samples MCM41, MCM41_ExE, MCM41_ExE_C, and MCM41_ExW. TEM images at a different magnification of the samples MCM41_ExE (c, d) and MCM41_ExW (e, f).

was further treated at 550 °C (MCM41_ExE_C) for 2 h, but a partial collapse of the porous structure occurred. Both the isotherm and the pore size distribution of the sample MCM41_ExW show a complete loss of the mesostructure centered at 2−3 nm (capillary condensation phenomena observed as steps in the range 0.1−0.3 P/P_0), typical for MCM-41. However, in the isotherm, a new contribution at

https://dx.doi.org/10.1021/acssuschemeng.0c03218
ACS Sustainable Chem. Eng. 2020, 8, 14286−14300

higher values of P/P_0 (0.7) due to the capillary condensation phenomena is observed, suggesting the presence of larger mesopores. These results prove that water is not a suitable solvent for the removal of the templating agent and the preservation of the mesostructure, probably because of possible reactions of silanol groups on the silica surface and water at the temperature at which the extraction was performed. The results of N_2-physisorption were further confirmed by TEM analysis: the sample MCM41_ExE retained its morphology in terms of size and shape of the particles as well as the porous order (Figure 5c,d), while the sample MCM41_ExW shows a worm-like mesoporous structure with pores in the size range of 10−30 nm (Figure 5e,f).

For comparison, also the as-synthesized TEOS_T50_3h_-Hyd sample was treated by 48 h of extraction with ethanol to recover the CTAB. In this case, the CTAB was not removed as demonstrated by the FTIR spectrum (Figure S8a). Therefore, another attempt was carried out by an extraction with ethanol/HCl solution, as suggested in the literature.[33] The 24 h extraction by ethanol/HCl solution was successful in that purpose (Figure S8a) but a partial collapse of the mesostructure occurred also before calcination (Figure S8b, Table S1).

These findings suggest a limit in the employment of the FSA-derived MCM-41 to low temperature applications, if subjected to ethanol extraction for CTAB recovery. In the case of TEOS-derived MCM-41, ethanol extraction does not permit the complete removal of CTAB molecules and ethanol/HCl solution extraction causes the loss of the original mesostructure, even before calcination.

Study of the Thermal and Hydrothermal Stability. Thermal stability was assessed for both TEOS- and FSA-derived MCM-41, by treating the samples at 650 °C, 750 °C, 900 °C, and 950 °C (Figure 6). A gradual decrease of the (100) signal intensity with temperature was detected in the SA-XRD patterns for the TEOS-derived MCM-41 (Figure 6a), indicating a progressive loss of the mesoporous structure, with a complete collapse at 950 °C. Conversely, the mesoporous order was retained up to 900 °C for the FSA-derived MCM-41, while at 950 °C the partial collapse of the porous structure was observed in the SA-XRD (Figure 6c). Therefore, the samples treated at 550, 750, and 900 °C were also analyzed by N_2-physisorption (Figure 6b,d), confirming this trend. In particular, the isotherms of the TEOS-derived samples treated at 550 and 750 °C (Figure 6b) and the surface area values were similar (above 1000 $m^2\ g^{-1}$, Table S2), but with a decrease in the capillary condensation in the latter, ascribable to mesopores as shown in the pore size distribution (Figure S9a). The collapse of the mesoporous structure in the sample treated at 900 °C was confirmed also by this technique, with the absence of the capillary condensation between 0.2 and 0.3 P/P_0 and the corresponding pore size distribution (Figure S9a). The overlapping N_2-physisorption isotherms (Figure 6d) and pore size distributions (Figure S9b) of the samples treated at 550 and 750 °C further confirmed this finding with also similar values of specific surface area (about 800 $m^2\ g^{-1}$, Table S2). The sample treated at 900 °C kept the mesostructure, even if a partial collapse occurred accompanied by a small reduction of the surface area (from 825 $m^2\ g^{-1}$ to 748 $m^2\ g^{-1}$), as observed from the reduction of the capillary condensation phenomena.

Both samples were also tested for hydrothermal stability in water,[34] revealing a decrease in the mesopores' contribution of

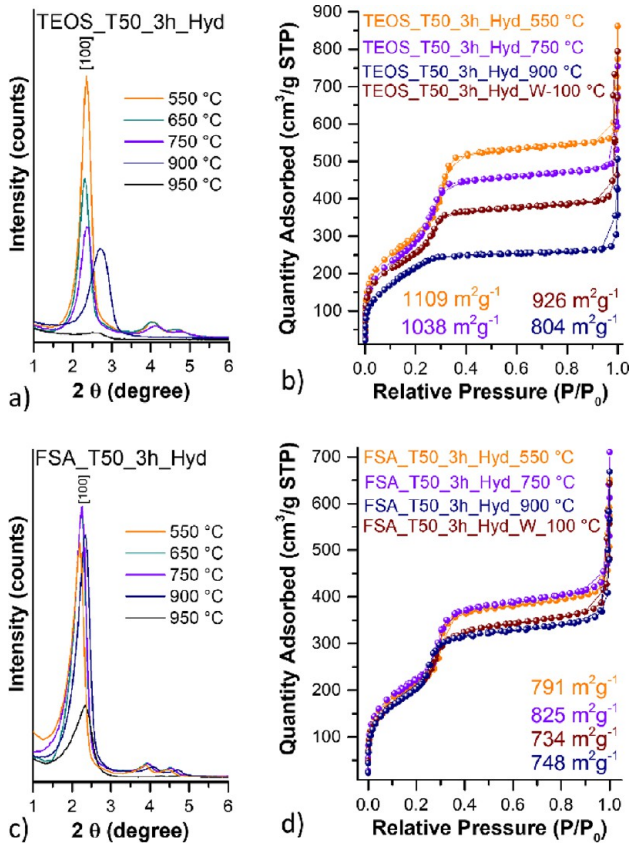

Figure 6. SA-XRD patterns (a,c and d,f) and N_2-physisorption isotherms (b, e), of TEOS- and FSA-derived MCM-41 treated at different temperature and by hydrothermal treatment.

the N_2-physisorption isotherms (Figure 6b, d), with a decrease in the surface area of 17% and 7% for the TEOS- and the FSA-derived MCM-41, respectively. However, these decreases are lower than that obtained by other authors (−29%).[34] The pore size distributions were also similar (Figure S9), centered at 2.5 nm (Table S2) but less intense with respect to the calcined samples.

Therefore, the FSA-derived MCM-41 sample showed better thermal and comparable hydrothermal stability than the TEOS-derived counterparts. This difference might be ascribed to a more robust mesoporous structure in the FSA-derived MCM-41, due to thicker walls (Table S2). Indeed, other authors showed a relationship between the thermal stability of the mesostructured and the wall thickness.[46,47]

FSA-MCM41 Support for Fe_2O_3-Based Composite As H_2S Remover. In light of these results, it is possible to claim that, despite the great differences in the chemical nature of the precursors, the samples obtained from TEOS and FSA feature similar surface areas, pore diameters, and pore size distributions, with the additional advantages of utilizing a hazardous waste material in the case of the FSA precursor and of achieving a more robust mesostructure with higher thermal stability. The previous sets of experiments were instrumental in determining the best conditions whereby it was possible to synthesize a mesostructured MCM-41 from FSA to be used as a host for anchoring active phases, through a nanocompositing process.[48] In fact, it has been already demonstrated by Cara et al. that Fe_2O_3_MCM-41 and Fe_2O_3_SBA15 materials made up of ultrasmall nanoparticles are efficient and regenerable sorbents for H_2S removal.[19,20,29,49] To verify whether an

https://dx.doi.org/10.1021/acssuschemeng.0c03218
ACS Sustainable Chem. Eng. 2020, 8, 14286−14300

FSA-derived MCM-41 support can serve as an alternative to its TEOS-derived counterpart in obtaining an equally efficient nanocomposite, the bare calcined FSA-derived MCM-41 (FSA_T50_3h_Hyd, here for simplicity labeled MCM41) was compared in terms of structural and textural properties with the TEOS-derived MCM-41 (here labeled as MCM41_Ref) proposed in a recent article,[49] while the corresponding nanocomposite was compared in terms of performances in H_2S removal.[19,49,50] For the development of the composite, the calcined FSA-MCM-41 was preferred over the ethanol-extracted sample, due to its higher thermal stability (see CTAB Recovery section).

^{29}Si MAS solid-state NMR spectroscopy was used to assess possible differences in terms of structural properties, i.e., different coordination of Si atoms, in terms of relative abundance of Q^2, Q^3, and Q^4 sites, between the FSA-derived sample (MCM41) and its TEOS-derived counterpart (MCM41_Ref). The collected spectra are reported in Figure 7.

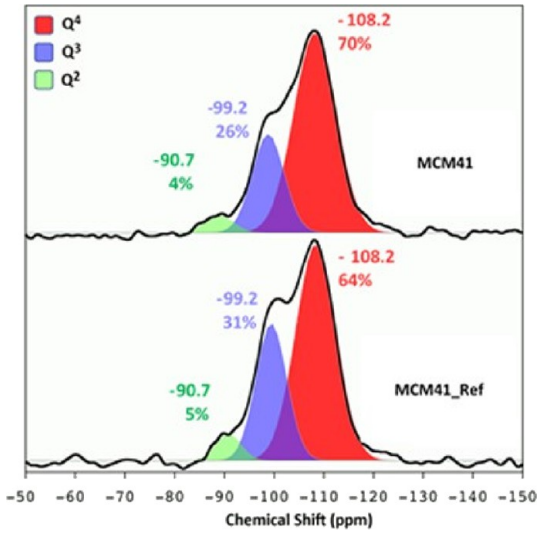

Figure 7. ^{29}Si MAS-solid-state NMR spectra of MCM41_Ref, from TEOS, and MCM41, from FSA, with the chemical shift (ppm) and peak relative area (%) of the three revealed resonances.

Both the spectra show three partially overlapped resonances centered at −90.7, −99.2, and −108.2 ppm ascribable to Q^2, Q^3, and Q^4 sites, respectively.[51] The deconvolution with Gaussian components allowed determination of the relative abundances of the three different silicon coordination states exhibited by the samples. The results highlight the structural similarity between the two samples (Figure 7), justified by the great similarity in surface area (877 $m^2\ g^{-1}$ and 886 $m^2\ g^{-1}$ for MCM41_Ref and MCM41, respectively) and pore size distribution (Table 3). Moreover, these values are also comparable to those reported in the literature for silicas treated at a similar temperature, including microporous, mesoporous, and mesostructured SiO_2.[52]

Figure 8 reports the results of the characterization of the nanocomposite (10Fe_ MCM41) in comparison with the bare MCM-41 (MCM41). The SA-XRD pattern of the composite (Figure 8a) is almost entirely superimposable with those of the bare sample showing the reflections (100), (110), and (200) typical of a long-range hexagonal order of the mesopores (space group *P6mm*). In the WA-XRD pattern, along with the typical reflection centered at 22° ascribable to amorphous

Table 3. Surface Area (S_{BET}), Pore Volume (V_P), DFT-Determined Pore Diameter ($D_{p(DFT)}$), Lattice Spacing (d_{100}), Hexagonal Unit Cell Parameter (a_0), and Wall Thickness (w_t) of the Bare Sample MCM41 (Corresponding to FSA_T50_3h_Hyd), the Fresh Composite (10Fe_MCM41), and the Three-Time Regenerated One (10Fe_MCM41_3R)[a]

sample	S_{BET} ($m^2\ g^{-1}$)	V_p ($cm^3\ g^{-1}$)	$D_{p(DFT)}$ (nm)	W_t (nm)	d_{100} (nm)	a_0 (nm)
MCM41_Ref *	877	0.7	3.4	1.0	3.8	4.4
10Fe_MCM41_Ref*	744	0.6	3.4	1.0	3.8	4.4
MCM41	886	0.7	3.6	0.8	3.8	4.4
10Fe_MCM41	754	0.6	3.6	0.7	3.8	4.4
10Fe_MCM41 _3R	685	0.7	3.6	0.7	3.8	4.4

[a]The * indicates values reported in reference 49. For comparison with the other samples, the D_p (DFT) of the MCM41_Ref and 10Fe_MCM41_Ref were recalculated using DFT model instead of BHJ.

silica, two weak broad reflections at 35° and 63° reveal the formation of a composite with a highly dispersed iron-containing phase (Figure 8b).[19,20,29,48,49] N_2-physisorption isotherm of the composite (Figure 8c) displays the typical IVB isotherm shape for a mesoporous material with pore size distribution centered at about 3.7 nm (Figure 8d). Pore diameter, wall thickness, d_{100}, and a_0 values of the composite are mostly identical to those of bare silica (Table 3). However, as expected, a reduction in the surface area (from 886 $m^2\ g^{-1}$ to 754 $m^2\ g^{-1}$) and pore volume (from 0.7 $cm^3\ g^{-1}$ to 0.6 $cm^3\ g^{-1}$) is observed upon impregnation and calcination.

To assess the nature of the active phase and verify how the textural properties of the matrix govern the final features of the iron-bearing phase, the combined use of RT ^{57}Fe Mössbauer spectroscopy, DC magnetometry, and HRTEM was performed on the composite.[19,20,48,49,53] The RT ^{57}Fe Mössbauer data (Figure S10a) as well as the DC magnetometry show similar features of the composites prepared from TEOS in previous works.[19,20] The doublet with an isomer shift of 0.34 ± 0.01 mm/s in the RT ^{57}Fe Mössbauer spectrum, the maximum in the ZFC curve at about 11 K (Figure S10b), and an S-shaped magnetic field dependence of the magnetization at 5 K (Figure S10c) are ascribable to ultrasmall maghemite nanoparticles[19,20] HRTEM allows to evidence the uniform distribution of the Fe-bearing active phase all over the support (Figure 8f) and the formation of well-crystallized spheroidal nanoparticles of about 2 nm having single interfringe distances of about 2 Å, ascribable to plane (400) of maghemite (γ-Fe_2O_3, PDF card no. 00-039-1346, 2.09 Å, intensity = 19%, Figure 8g), in agreement with ^{57}Fe Mössbauer spectroscopy and DC magnetometry data. HRTEM also confirmed the retention of the mesostructure upon impregnation with the two-solvent technique (Figure 8e).

To prove the H_2S removal capacity, the sorbent underwent three sulfidation−regeneration cycles (Figure S11, Table S3). The H_2S removal performances of 10Fe_MCM41, expressed in terms of sulfur retention capacity (SRC) of the three sulfidation runs, are reported in Figure 9 and Table S3 and were compared with those of 10Fe_MCM41_Ref. The samples show similar performances, featuring steady behavior over the three sulfidation runs (Figure 9) with slightly lower and similar SRC values (about 20 $mg_S\ g_{sorbent}^{-1}$) in the second and third cycles, that can be probably explained due to the

https://dx.doi.org/10.1021/acssuschemeng.0c03218
ACS Sustainable Chem. Eng. 2020, 8, 14286−14300

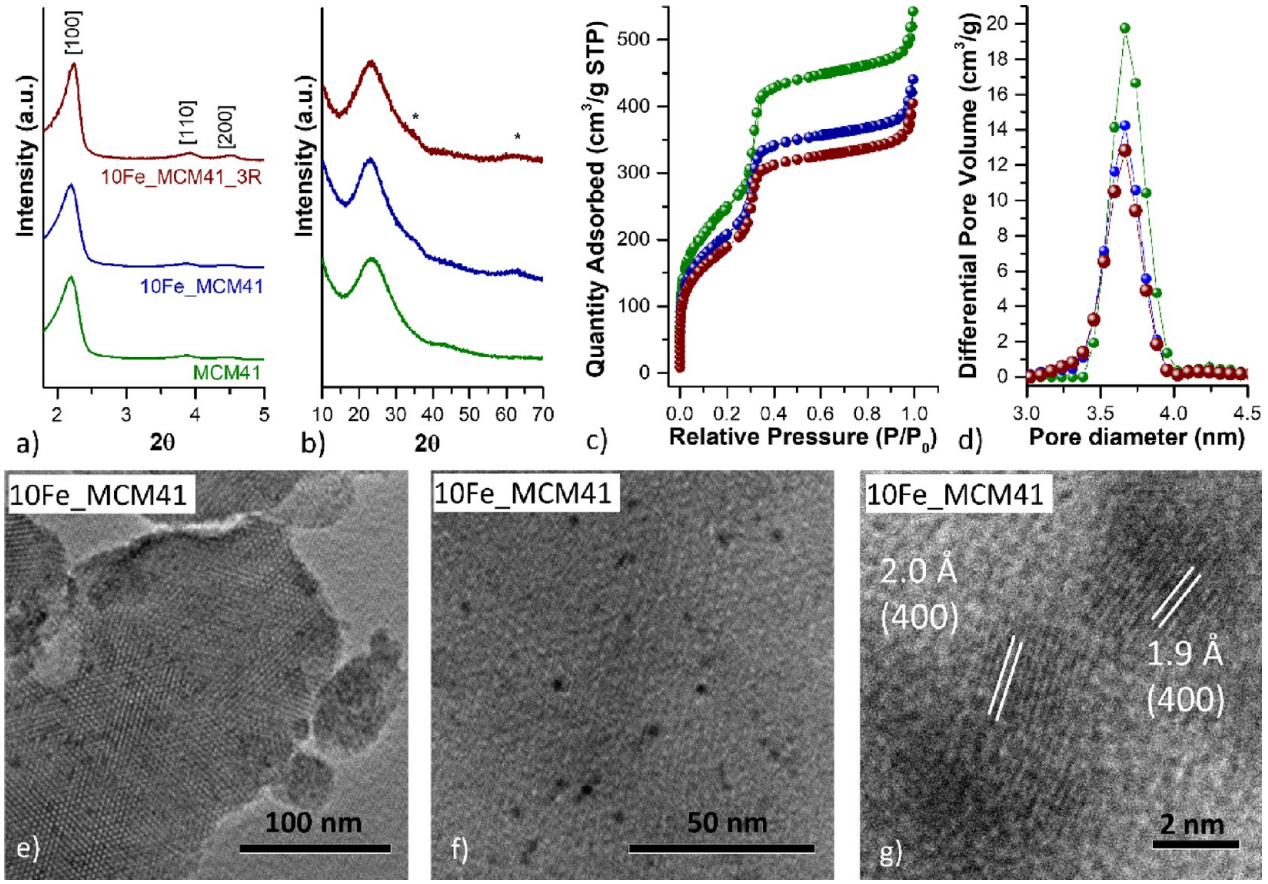

Figure 8. SA- and WA-XRD patterns (a, b), N_2-physisorption isotherms (c), and pore size distributions (d) of FSA-derived MCM-41 and its 10% w/w Fe_2O_3 nanocomposite in the fresh (10Fe_MCM41) and regenerated (10Fe_MCM41_3R) state. HRTEM micrographs of the sample 10Fe_MCM41 at different magnifications (e, f) and interfringe distances with corresponding Miller's indexes (g).

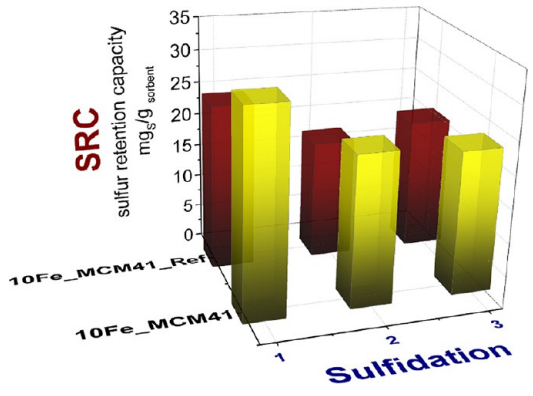

Figure 9. H_2S removal performances of 10Fe_MCM41 derived from FSA compared with 10Fe_MCM41_Ref derived from TEOS.

transition of ultrasmall maghemite to hematite nanoparticles, as evidenced for the sample MCM41_Ref.[49]

After the three regeneration−sulfidation cycles, the resulting sample (10Fe_MCM41_3R) was characterized through SA-XRD and N_2-physisorption measurements, to assess whether it retained its structural and textural properties (Figure 8). The SA-XRD pattern shows the three typical reflections of an MCM-41 material, indicating the preservation of the hexagonal mesoporous order over the three regeneration−sulfidation cycles (Figure 8a). N_2-physisorption measurements (Figure 8c) also confirmed the retention of the textural properties: similar values for pore volume, pore diameter, and very similar pore size distribution were found (Table 3, Figure 8d), although a decrease of 10% in the value of the surface area was observed, as in the case of sorbents derived from MCM41_Ref.[19,20,50] These findings highlight the feasibility of FSA as an alternative silica source to obtain high value-added mesostructured siliceous materials, to be efficiently used as supports of active phases in environmental applications such as H_2S removal from sour syngas and in other applications in which gas−solid or liquid−solid reactions are involved.

CONCLUSIONS

Hexafluorosilicic acid (H_2SiF_6 or FSA), an industrial waste mainly deriving from the fertilizer industry and the production of HF, was proved to be an excellent substitute for the common Si-containing precursors (alkoxides) in the synthesis of highly ordered mesostructured silicas, such as MCM-41. The high value added by MCM-41 samples deriving from FSA was proven by means of a systematic head-to-head comparison between TEOS- and FSA-derived materials. Such a comparison demonstrated that the typical features of high-quality mesostructured silica, such as high surface area, narrow pore size distribution, a high degree of porous order, and amount of Q_2, Q_3, and Q_4 sites, were comparable to those shown by TEOS-derived MCM-41 materials. Higher thermal and comparable hydrothermal stabilities were revealed for the calcined FSA-derived MCM-41 with respect to the TEOS counterpart, suggesting possible application in mid- and high-temperature applications. The high value of FSA-derived

https://dx.doi.org/10.1021/acssuschemeng.0c03218
ACS Sustainable Chem. Eng. 2020, 8, 14286−14300

mesostructured silica was also revealed by its capacity to homogeneously disperse an active phase in the form of ultrasmall Fe_2O_3 nanoparticles, which are easily accessible to gaseous species, such as H_2S. This may pave the way to the use of calcined FSA-derived mesostructured materials as ideal matrices for anchoring small inorganic nanoentities or organic molecules in a variety of applications, where gas−solid or liquid−solid interfaces are concerned. Exploiting the nature of FSA as both a silicon and fluorine source, after the synthesis of MCM-41, nanostructured fluorite (CaF_2) was also obtained as an additional valuable product by treating the mother solution (ammonium fluoride solution) with calcium hydroxide. This process permitted the recovery of the CTAB-rich ammonia solution, which can be employed for successive synthesis with FSA. Furthermore, the recovery of CTAB molecules entrapped in the MCM-41 mesostructure can be also obtained by ethanol extraction in the case of FSA-MCM-41 but leading to a less thermally stable material in comparison with the calcined one that can be only used for low temperature applications. The utilization of a waste as the silicon source and the opportunity to produce CaF_2 and recover ammonia and CTAB may be instrumental in designing an efficient process, abiding by the dictates of both green chemistry and blue economy.

■ ASSOCIATED CONTENT

Supporting Information

The Supporting Information is available free of charge at https://pubs.acs.org/doi/10.1021/acssuschemeng.0c03218.

Flowchart of the synthetic route, BJH and DFT pore size distribution, fluorite recovery, effect of time, effect of ethyl acetate and hydrothermal treatment, CTAB recovery, thermal and hydrothermal stability, characterization of the iron-bearing active phase, H_2S removal test (PDF)

■ AUTHOR INFORMATION

Corresponding Author

Carla Cannas − *University of Cagliari, Department of Chemical Science, 09042 Monserrato, Italy; Consorzio Interuniversitario Nazionale per La Scienza e Tecnologia Dei Materiali (INSTM), Firenze 50121, Italy;* orcid.org/0000-0003-2908-7739; Email: ccannas@unica.it

Authors

Mirko Antonio Vacca − *University of Cagliari, Department of Chemical Science, 09042 Monserrato, Italy*

Claudio Cara − *University of Cagliari, Department of Chemical Science, 09042 Monserrato, Italy; Consorzio Interuniversitario Nazionale per La Scienza e Tecnologia Dei Materiali (INSTM), Firenze 50121, Italy*

Valentina Mameli − *University of Cagliari, Department of Chemical Science, 09042 Monserrato, Italy; Consorzio Interuniversitario Nazionale per La Scienza e Tecnologia Dei Materiali (INSTM), Firenze 50121, Italy;* orcid.org/0000-0002-1899-8636

Marco Sanna Angotzi − *University of Cagliari, Department of Chemical Science, 09042 Monserrato, Italy; Consorzio Interuniversitario Nazionale per La Scienza e Tecnologia Dei Materiali (INSTM), Firenze 50121, Italy;* orcid.org/0000-0003-1593-5872

Mariano Andrea Scorciapino − *University of Cagliari, Department of Chemical Science, 09042 Monserrato, Italy;* orcid.org/0000-0001-7502-7265

Maria Giorgia Cutrufello − *University of Cagliari, Department of Chemical Science, 09042 Monserrato, Italy*

Anna Musinu − *University of Cagliari, Department of Chemical Science, 09042 Monserrato, Italy; Consorzio Interuniversitario Nazionale per La Scienza e Tecnologia Dei Materiali (INSTM), Firenze 50121, Italy*

Vaclav Tyrpekl − *Charles University in Prague, Department of Inorganic Chemistry, 12843 Prague 2, Czech Republic;* orcid.org/0000-0001-7149-1343

Luca Pala − *Fluorsid S.p.A, Assemini 09032, Italy*

Complete contact information is available at: https://pubs.acs.org/10.1021/acssuschemeng.0c03218

Author Contributions

⊥These authors contributed equally.

Notes

The authors declare no competing financial interest.

■ ACKNOWLEDGMENTS

We are grateful for the support of Franca Sini in the N_2-physisorption measurements. MIUR − National Program PON Ricerca e Innovazione 2014-2020 is acknowledged for the Ph.D. grant of Mirko Antonio Vacca. RAS-Piano Sulcis (CESA and V-Fase Projects), Fluorsid S.p.A., and PON AIM (PON Ricerca e Innovazione 2014−2020 - Azione I.2 - D.D. n.407 del 27 febbraio 2018 "Attraction and International Mobility," Cult-GeoChim project AIM1890410-3) are gratefully acknowledged for financing the fellowships of M. Sanna Angotzi, C. Cara, and V. Mameli, respectively. We acknowledge the CeSAR (Centro Servizi d'Ateneo per la Ricerca) of the University of Cagliari, Italy for the DC magnetometry experiments performed with Quantum Design PMS DynaCool, for the TEM and HRTEM measurements performed with JEOL JEM 1400 PLUS and JEOL JEM 2010 UHR, and for the ^{29}Si-MAS solid-state NMR analyses performed with Bruker Avance III HD spectrometer.

■ REFERENCES

(1) Dahlke, T.; Ruffiner, O.; Cant, R. Production of HF from H_2SiF_6. *Procedia Eng.* **2016**, *138*, 231−239.
(2) *Ullmann's Encyclopedia of Industrial Chemistry*, 7th ed.; Wiley, 2000; DOI: 10.1002/14356007.
(3) Will, R. K. The Benefits of Isolating & Utilizing Fluorine from Phosphate Operations. *Procedia Eng.* **2016**, *138*, 267−272.
(4) Toure, A. O.; Sambe, F. M.; Koita, D.; Diop, C. M. G.; Sock, O. Processes for Working-up an Aqueous Fluosilicic Acid Solution. *S. Afr. J. Sci.* **2012**, *108* (11/12), 1−5.
(5) Dreveton, A. Manufacture of Aluminium Fluoride of High Density and Anhydrous Hydrofluoric Acid from Fluosilicic Acid. *Procedia Eng.* **2012**, *46*, 255−265.
(6) Pala, L.; Lavanga, M. High Purity Synthetic Fluorite, Process for Preparing the Same and Apparatus Therefor. WO2016/156969Al, 2016.
(7) Yu, H. S.; Rhee, K.-I.; Lee, C. K.; Yang, D.-H. Two-Step Ammoniation of by-Product Fluosilicic Acid to Produce High Quality Amorphous Silica. *Korean J. Chem. Eng.* **2000**, *17* (4), 401−408.
(8) Liu, T.; Jin, F.; Wang, X.; Fan, Y.; Yuan, M. Synthesis of Titanium Containing MCM-41 from Industrial Hexafluorosilicic Acid as Epoxidation Catalyst. *Catal. Today* **2017**, *297*, 316−323.
(9) Elineema, G.; Kim, J. K.; Hilonga, A.; Shao, G. N.; Kim, Y.-N.; Quang, D. V.; Sarawade, P. B.; Kim, H. T. Quantitative Recovery of

High Purity Nanoporous Silica from Waste Products of the Phosphate Fertilizer Industry. *J. Ind. Eng. Chem.* **2013**, *19* (1), 63−67.
(10) Sarawade, P. B.; Kim, J.-K.; Hilonga, A.; Kim, H. T. Recovery of High Surface Area Mesoporous Silica from Waste Hexafluorosilicic Acid (H_2SiF_6) of Fertilizer Industry. *J. Hazard. Mater.* **2010**, *173* (1−3), 576−580.
(11) Zhao, D.; Feng, J.; Huo, Q.; Melosh, N.; Fredrickson, G. H.; Chmelka, B. F.; Stucky, G. D. Triblock Copolymer Syntheses of Mesoporous Silica with Periodic 50 to 300 Angstrom Pores. *Science (Washington, DC, U. S.)* **1998**, *279* (5350), 548−552.
(12) Varghese, S.; Cutrufello, M. G.; Rombi, E.; Cannas, C.; Monaci, R.; Ferino, I. CO Oxidation and Preferential Oxidation of CO in the Presence of Hydrogen over SBA-15-Templated CuO-Co3O4 Catalysts. *Appl. Catal., A* **2012**, *443−444*, 161−170.
(13) Rombi, E.; Cutrufello, M. G.; Cannas, C.; Casu, M.; Gazzoli, D.; Occhiuzzi, M.; Monaci, R.; Ferino, I. Modifications Induced by Pretreatments on Au/SBA-15 and Their Influence on the Catalytic Activity for Low Temperature CO Oxidation. *Phys. Chem. Chem. Phys.* **2009**, *11* (3), 593−602.
(14) Taguchi, A.; Schüth, F. Ordered Mesoporous Materials in Catalysis. *Microporous Mesoporous Mater.* **2005**, *77* (1), 1−45.
(15) Martin, T.; Galarneau, A.; Di Renzo, F.; Brunel, D.; Fajula, F.; Heinisch, S.; Crétier, G.; Rocca, J.-L. Great Improvement of Chromatographic Performance Using MCM-41 Spheres as Stationary Phase in HPLC. *Chem. Mater.* **2004**, *16* (9), 1725−1731.
(16) Bharti, C.; Gulati, N.; Nagaich, U.; Pal, A. Mesoporous Silica Nanoparticles in Target Drug Delivery System: A Review. *Int. J. Pharm. Investig.* **2015**, *5* (3), 124.
(17) Giraldo, L. F.; López, B. L.; Pérez, L.; Urrego, S.; Sierra, L.; Mesa, M. Mesoporous Silica Applications. *Macromol. Symp.* **2007**, *258* (1), 129−141.
(18) Yantasee, W.; Rutledge, R. D.; Chouyyok, W.; Sukwarotwat, V.; Orr, G.; Warner, C. L.; Warner, M. G.; Fryxell, G. E.; Wiacek, R. J.; Timchalk, C.; Addleman, R. S. Functionalized Nanoporous Silica for the Removal of Heavy Metals from Biological Systems: Adsorption and Application. *ACS Appl. Mater. Interfaces* **2010**, *2* (10), 2749−2758.
(19) Cara, C.; Rombi, E.; Mameli, V.; Ardu, A.; Sanna Angotzi, M.; Niznansky, D.; Musinu, A.; Cannas, C. γ-Fe_2O_3 -M41S Sorbents for H_2S Removal: Effect of Different Porous Structures and Silica Wall Thickness. *J. Phys. Chem. C* **2018**, *122* (23), 12231−12242.
(20) Cara, C.; Rombi, E.; Musinu, A.; Mameli, V.; Ardu, A.; Sanna Angotzi, M.; Atzori, L.; Niznansky, D.; Xin, H. L.; Cannas, C. MCM-41 Support for Ultrasmall γ-Fe 2 O 3 Nanoparticles for H_2S Removal. *J. Mater. Chem. A* **2017**, *5* (41), 21688−21698.
(21) Kresge, C. T.; Leonowicz, M. E.; Roth, W. J.; Vartuli, J. C.; Beck, J. S. Ordered Mesoporous Molecular Sieves Synthesized by a Liquid-Crystal Template Mechanism. *Nature* **1992**, *359* (6397), 710−712.
(22) Bhagiyalakshmi, M.; Yun, L. J.; Anuradha, R.; Jang, H. T. Utilization of Rice Husk Ash as Silica Source for the Synthesis of Mesoporous Silicas and Their Application to CO_2 Adsorption through TREN/TEPA Grafting. *J. Hazard. Mater.* **2010**, *175* (1−3), 928−938.
(23) Boonpoke, A.; Chiarakorn, S.; Laosiripojana, N.; Towprayoon, S.; Chidthaisong, A. Synthesis of Activated Carbon and MCM-41 from Bagasse and Rice Husk and Their Carbon Dioxide Adsorption Capacity. *J. Sustain. Energy Environ.* **2011**, *2*, 77−81.
(24) Ghorbani, F.; Younesi, H.; Mehraban, Z.; Çelik, M. S.; Ghoreyshi, A. A.; Anbia, M. Preparation and Characterization of Highly Pure Silica from Sedge as Agricultural Waste and Its Utilization in the Synthesis of Mesoporous Silica MCM-41. *J. Taiwan Inst. Chem. Eng.* **2013**, *44* (5), 821−828.
(25) Hui, K. S.; Chao, C. Y. H. Synthesis of MCM-41 from Coal Fly Ash by a Green Approach: Influence of Synthesis PH. *J. Hazard. Mater.* **2006**, *137* (2), 1135−1148.
(26) Misran, H.; Singh, R.; Begum, S.; Yarmo, M. A. Processing of Mesoporous Silica Materials (MCM-41) from Coal Fly Ash. *J. Mater. Process. Technol.* **2007**, *186* (1−3), 8−13.
(27) Jeong, S.; Suh, J.; Lee, J.; Kwon, O. Preparation of Silica-Based Mesoporous Materials From Fluorosilicon Compounds: Gelation of H_2SiF_6 in Ammonia Surfactant Solution. *J. Colloid Interface Sci.* **1997**, *192* (1), 156−161.
(28) Liou, T. A Green Route to Preparation of MCM-41 Silicas with Well-Ordered Mesostructure Controlled in Acidic and Alkaline Environments. *Chem. Eng. J.* **2011**, *171* (3), 1458−1468.
(29) Mureddu, M.; Ferino, I.; Musinu, A.; Ardu, A.; Rombi, E.; Cutrufello, M. G.; Deiana, P.; Fantauzzi, M.; Cannas, C. MeO x /SBA-15 (Me = Zn, Fe): Highly Efficient Nanosorbents for Mid-Temperature H_2S Removal. *J. Mater. Chem. A* **2014**, *2* (45), 19396−19406.
(30) Brinton, P. H. M. P.; Sarver, L. A.; Stoppel, A. E. The Titration of Hydrofluoric and Hydrofluosilicic Acids in Mixtures Containing Small Amounts of Hydrofluosilicic Acid. *Ind. Eng. Chem.* **1923**, *15* (10), 1080−1081.
(31) Mureddu, M.; Ferino, I.; Rombi, E.; Cutrufello, M. G.; Deiana, P.; Ardu, A.; Musinu, A.; Piccaluga, G.; Cannas, C. ZnO/SBA-15 Composites for Mid-Temperature Removal of H_2S: Synthesis, Performance and Regeneration Studies. *Fuel* **2012**, *102*, 691−700.
(32) Du, P. D.; Khieu, D. Q.; Hoa, T. T. Removal of Organic Template from Mesoporous MCM-41. *Hue Univ. J. Sci.* **2011**, *69* (6), 35−41.
(33) Kumar, P.; Ida, J.; Kim, S.; Guliants, V. V.; Lin, J. Y. S. Ordered Mesoporous Membranes: Effects of Support and Surfactant Removal Conditions on Membrane Quality. *J. Membr. Sci.* **2006**, *279* (1−2), 539−547.
(34) Chen, L. Y.; Jaenicke, S.; Chuah, G. K. Thermal and Hydrothermal Stability of Framework-Substituted MCM-41 Mesoporous Materials. *Microporous Mater.* **1997**, *12* (4−6), 323−330.
(35) Thommes, M.; Köhn, R.; Fröba, M. Sorption and Pore Condensation Behavior of Pure Fluids in Mesoporous MCM-48 Silica, MCM-41 Silica, SBA-15 Silica and Controlled-Pore Glass at Temperatures above and below the Bulk Triple Point. *Appl. Surf. Sci.* **2002**, *196* (1−4), 239−249.
(36) Eyal Aharon, M. Recovery of Ammonia and Hydrogen Fluoride from Ammonium Fluoride Solutions. US0 286 449A1, 1988.
(37) Morita, M.; Granata, G.; Tokoro, C. Recovery of Calcium Fluoride from Highly Contaminated Fluoric/Hexafluorosilicic Acid Wastewater. *Mater. Trans.* **2018**, *59* (2), 290−296.
(38) Rouquerol, J.; Françoise, R.; Phillip, L.; Guillaume, M.; Kenneth, S. *Adsorption by Powders and Porous Solids*, 2nd ed.; Elsevier, 1999; DOI: 10.1016/B978-0-12-598920-6.X5000-3.
(39) Zhao, D.; Wan, Y.; Zhou, W. *Ordered Mesoporous Materials*; Wiley-VCH Verlag GmbH & Co. KGaA: Weinheim, Germany, 2013; Vol. *27*; DOI: 10.1002/9783527647866.
(40) Meléndez-Ortiz, H. I.; García-Cerda, L. A.; Olivares-Maldonado, Y.; Castruita, G.; Mercado-Silva, J. A.; Perera-Mercado, Y. A. Preparation of Spherical MCM-41 Molecular Sieve at Room Temperature: Influence of the Synthesis Conditions in the Structural Properties. *Ceram. Int.* **2012**, *38* (8), 6353−6358.
(41) Fulvio, P. F.; Pikus, S.; Jaroniec, M. Tailoring Properties of SBA-15 Materials by Controlling Conditions of Hydrothermal Synthesis. *J. Mater. Chem.* **2005**, *15* (47), 5049.
(42) Yantasee, W.; Rutledge, R. D.; Chouyyok, W.; Sukwarotwat, V.; Orr, G.; Warner, C. L.; Warner, M. G.; Fryxell, G. E.; Wiacek, R. J.; Timchalk, C.; Addleman, R. S. Functionalized Nanoporous Silica for the Removal of Heavy Metals from Biological Systems: Adsorption and Application. *ACS Appl. Mater. Interfaces* **2010**, *2* (10), 2749−2758.
(43) Suteewong, T.; Sai, H.; Lee, J.; Bradbury, M.; Hyeon, T.; Gruner, S. M.; Wiesner, U. Ordered Mesoporous Silica Nanoparticles with and without Embedded Iron Oxide Nanoparticles: Structure Evolution during Synthesis. *J. Mater. Chem.* **2010**, *20* (36), 7807.
(44) Ng, E.; Goh, J.; Ling, T. C.; Mukti, R. R. Eco-Friendly Synthesis for MCM-41 Nanoporous Materials Using the Non-Reacted Reagents in Mother Liquor. *Nanoscale Res. Lett.* **2013**, *8* (1), 120.

(45) Prasomsri, T.; Jiao, W.; Weng, S. Z.; Garcia Martinez, J. Mesostructured Zeolites: Bridging the Gap between Zeolites and MCM-41. *Chem. Commun.* **2015**, *51* (43), 8900−8911.
(46) AlOthman, Z. A.; Apblett, A. W. Synthesis and Characterization of a Hexagonal Mesoporous Silica with Enhanced Thermal and Hydrothermal Stabilities. *Appl. Surf. Sci.* **2010**, *256* (11), 3573−3580.
(47) Yu, J.; Shi, J.-L.; Wang, L.-Z.; Ruan, M.-L.; Yan, D.-S. Preparation of High Thermal Stability MCM-41 in the Low Surfactant/Silicon Molar Ratio Synthesis Systems. *Mater. Lett.* **2001**, *48* (2), 112−116.
(48) Mameli, V.; Musinu, A.; Niznansky, D.; Peddis, D.; Ennas, G.; Ardu, A.; Lugliè, C.; Cannas, C. Much More Than a Glass: The Complex Magnetic and Microstructural Properties of Obsidian. *J. Phys. Chem. C* **2016**, *120* (48), 27635−27645.
(49) Cara, C.; Mameli, V.; Rombi, E.; Pinna, N.; Sanna Angotzi, M.; Nižňanský, D.; Musinu, A.; Cannas, C. Anchoring Ultrasmall Fe^{III}-Based Nanoparticles on Silica and Titania Mesostructures for Syngas H_2S Purification. *Microporous Mesoporous Mater.* **2020**, *298*, 110062.
(50) Cara, C.; Rombi, E.; Ardu, A.; Vacca, M. A.; Cannas, C. Sub-Micrometric MCM-41 Particles as Support to Design Efficient and Regenerable Maghemite-Based Sorbent for H_2S Removal. *J. Nanosci. Nanotechnol.* **2019**, *19* (8), 5035−5042.
(51) Lippmaa, E.; Maegi, M.; Samoson, A.; Engelhardt, G.; Grimmer, A. R. Structural Studies of Silicates by Solid-State High-Resolution Silicon-29 NMR. *J. Am. Chem. Soc.* **1980**, *102* (15), 4889−4893.
(52) Steel, A.; Carr, S. W.; Anderson, M. W. 29Si Solid-State NMR Study of Mesoporous M41S Materials. *Chem. Mater.* **1995**, *7* (10), 1829−1832.
(53) Mameli, V.; Angotzi, M. S.; Cara, C.; Cannas, C. Liquid Phase Synthesis of Nanostructured Spinel Ferrites—A Review. *J. Nanosci. Nanotechnol.* **2019**, *19* (8), 4857−4887.

https://dx.doi.org/10.1021/acssuschemeng.0c03218
ACS Sustainable Chem. Eng. 2020, 8, 14286−14300